3.2. The physics of diffraction from powders

P. W. STEPHENS

3.2.1. Introduction

The term powder is used here as a label for polycrystalline samples, but they may not be powdery at all, *e.g.*, metallurgical samples or chocolate. The central premise of powder diffraction is that the sample consists of a sufficiently large number of independent particles (Smith, 2001). In that case, the diffraction pattern will consist of a series of peaks corresponding to the Bragg reflections from each component of the sample. This chapter starts with an idealized description of the data collected in a powder-diffraction measurement and how it relates to the physical properties of the sample and the diffractometer. In real experiments, many of the idealizations of this description are not satisfied, and the influence of those deviations from simple model behaviour are discussed in turn. To a greater or lesser extent, those confounding factors are under the control of the experimenter, and so it is important to understand how they can be optimized or avoided in the experimental design, as well as how to deal with situations where they cannot be (or have not been) avoided and deal with them in real data that have been collected.

The diffraction probes discussed here are X-rays and neutrons. Bragg's equation, $\lambda = 2d \sin \theta$, relates properties of the measurement (wavelength of the diffracted radiation λ and scattering angle 2θ) with a property of the sample (the d-spacing of the particular reflection observed). Data may be collected with radiation of fixed wavelength as a function of angle, or as energy-dispersive measurements at fixed angle. The former case is perhaps the most familiar, exemplified by a laboratory powder diffractometer using characteristic radiation from an X-ray tube, but it is frequently performed with X-rays or neutrons from a continuum source (*e.g.*, storage ring or nuclear reactor) selected by a suitable monochromator. Energy-dispersive X-ray experiments are performed by illuminating the sample with a continuum spectrum from a synchrotron source or *Bremsstrahlung* from an X-ray tube, whereas time-of-flight methods are in use at pulsed spallation neutron sources. Convenient conversions are that X-rays of energy E (keV) have wavelength λ (Å) = 12.398/E, and neutrons with a speed v (m s^{-1}) have wavelength λ (Å) = 3956/v.

3.2.2. Idealized diffraction from powders

From an experimental measurement, powder-diffraction data generally consist of detected intensity *versus* an experimental parameter (angle, time of flight, photon energy), where the latter can be related to the d-spacing of a Bragg reflection in the sample. Unless the sample is severely disordered, these data takes the form of a series of peaks which may or may not be distinctly separated. (In a severely disordered sample, the concept of a discrete set of Bragg peaks may not be applicable, and the Debye scattering equation, mentioned in Section 3.2.4 and more thoroughly covered in Chapters 3.6, 5.6 and 5.7, may be more appropriate.) The attributes of those peaks are their positions, integrated intensities and shapes. Their positions will depend on the dimensions of the crystal lattice, their relative intensities will depend on the crystallographic structure factors of the reflections, and their shapes will depend on aspects of the sample (*e.g.* grain size and internal strain) and on the configuration of the instrument on which the pattern is measured. We consider each of these in turn in the following sections.

In addition, there is generally a relatively smooth background (Riello *et al.*, 1995) due to a number of effects, such as fluorescence (X-rays), thermal diffuse scattering, multiple scattering within the sample, incoherent scattering, small-angle scattering, parasitic scattering from the atmosphere, the sample holder and/or the windows of environmental chambers, *etc.*

3.2.2.1. *Peak positions*

Starting with a single crystal, the lattice is described by non-coplanar translation vectors $\mathbf{a}, \mathbf{b}$ and $\mathbf{c}$, with magnitudes a, b and c, respectively, and angles α between $\mathbf{b}$ and $\mathbf{c}$, β between $\mathbf{c}$ and $\mathbf{a}$, and γ between $\mathbf{a}$ and $\mathbf{b}$. Diffraction peak positions are governed by the reciprocal lattice, spanned by vectors $\mathbf{a}^* = \mathbf{b} \times \mathbf{c}/(\mathbf{a} \cdot \mathbf{b} \times \mathbf{c})$ and cyclic permutations. These have the property that $\mathbf{a}^* \cdot \mathbf{a} = 1$, $\mathbf{b}^* \cdot \mathbf{a} = 0$ *etc.* (This is the 'crystallographic' convention; the scattering community usually defines reciprocal-lattice vectors as larger by a factor of 2π.) The reciprocal lattice is indexed by Miller indices (hkl), so that each vector in the reciprocal lattice is given by $\mathbf{G} = h\mathbf{a}^* + k\mathbf{b}^* + l\mathbf{c}^*$.

Incoming and diffracted radiation are described by wave vectors $\mathbf{k}_i$ and $\mathbf{k}_f$, both of magnitude $1/\lambda$, and separated by the angle 2θ. The condition for a particular Bragg reflection to be observed is $\mathbf{G}_{hkl} = \mathbf{k}_f - \mathbf{k}_i$. Note that this requires that the diffracting crystal be correctly oriented relative to the incident beam. For a given reflection $\mathbf{G}_{hkl}$, the d-spacing between reflecting planes is given by $d = 1/|\mathbf{G}|$. (Again, in the scattering convention, incident and diffracted beams have wave vectors of magnitude $2\pi/\lambda$, and $d = 2\pi/|\mathbf{G}|$.) In either case, this allows the Bragg condition to be written in the scalar form $\lambda = 2d \sin \theta$.

If the sample is a powder instead of a single crystal, some large number of crystallites will be aligned to meet the (vector) Bragg condition with the incident radiation, and then the diffracted radiation will take the form of a cone of opening half-angle 2θ.

It is often convenient to work with equations written for scalars, *viz.*

$$a^* = bc \sin \alpha / V,$$
$$\sin \alpha^* = V/(abc \sin \beta \sin \gamma) \text{ or equivalently}$$
$$\cos \alpha^* = \frac{\cos \beta \cos \gamma - \cos \alpha}{\sin \beta \sin \gamma},$$

with cyclic permutations. Here the unit-cell volume is given by

$$V = abc(1 - \cos^2 \alpha - \cos^2 \beta - \cos^2 \gamma + 2 \cos \alpha \cos \beta \cos \gamma)^{1/2}.$$

Note that the volume of the reciprocal cell is $V^* = 1/V$, and that the equations above are valid upon exchanging starred and unstarred variables.

For powder samples, using only scalars, the Bragg condition may be written as

$$\frac{4\sin^2\theta}{\lambda^2} = d^{-2} = Ah^2 + Bk^2 + Cl^2 + Dkl + Ehl + Fhk, \quad (3.2.1)$$

where $A = a^{*2}$, $B = b^{*2}$, $C = c^{*2}$, $D = 2b^*c^*\cos\alpha^*$, $E = 2c^*a^*\cos\beta^*$ and $F = 2a^*b^*\cos\gamma^*$. Crystal symmetries higher than triclinic lead to significant simplifications in the above, *e.g.* in the orthorhombic system, $a^* = 1/a$, $A = 1/a^2$ *etc.*, $\alpha^* = \beta^* = \gamma^* = 90°$, and $D = E = F = 0$. See Chapter 1.1, *Reciprocal space in crystallography*, in Volume B of *International Tables for Crystallography* for more details.

3.2.2.2. Diffraction peak intensities

3.2.2.2.1. X-rays

Consider a polycrystalline sample of randomly oriented grains of a single crystalline phase, containing a total number of atoms N, illuminated by an X-ray beam of wavelength λ. Each reciprocal-lattice vector with magnitude $|\mathbf{G}| < 2/\lambda$ will produce a cone of diffracted radiation with opening half-angle $2\theta = 2\sin^{-1}(\lambda|\mathbf{G}|/2)$. Regarding the diffraction lines as perfectly sharp delta-functions, the differential cross section for one powder Bragg peak is (Marshall & Lovesey, 1971)

$$\frac{d\sigma}{d\Omega} = \frac{N\lambda^3 r_e^2}{16\pi V} \frac{Pm_{hkl}}{\sin\theta\sin 2\theta} |A_{hkl}|^2 \delta\left(2\theta - 2\sin^{-1}\frac{\lambda}{2d}\right). \quad (3.2.2)$$

In this equation, $r_e = 2.82 \times 10^{-15}$ m is the classical electron radius and V is the unit-cell volume; the polarization factor P, multiplicity m_{hkl} and structure factor A_{hkl} are discussed below. Finite crystallite size, strain and other factors discussed below will broaden the peak, but the integrated intensity of each peak will be given by the factors before the delta-function.

Before continuing, note that this result is correct within the approximation that the entire sample is uniformly bathed in radiation (*i.e.*, there is no absorption) and the kinematic approximation that the scattering power is very weak, so that further interaction of the scattered radiation with the sample may be neglected. The latter is equivalent to the Born approximation of elementary quantum mechanics, and its failure is referred to as extinction; it is discussed below in Section 3.2.3.6. It should also be noted here that equation (3.2.2) refers only to diffraction in Bragg peaks, and not to thermal diffuse scattering or scattered radiation due to static distortions from an ideal crystal lattice (Huang scattering; Krivoglaz, 1969).

Returning to the terms in equation (3.2.2), for X-rays the polarization factor P accounts for the polarization dependence of the Thomson scattering cross section from a free electron. For a completely polarized incident beam: $P = 1$ for S polarization (polarization perpendicular to the scattering plane); $P = \cos^2 2\theta$ for P polarization (in the scattering plane). For unpolarized X-rays (no monochromator), $P = (1 + \cos^2 2\theta)/2$. For horizontally polarized X-rays from a synchrotron-radiation source, diffracted vertically, the polarization factor is very close to unity, and so P can generally be taken as 1. If there is a crystal monochromator (deflection angle $2\theta_m$) coplanar with the diffractometer and an unpolarized source, $P = (1 + \cos^2 2\theta_m \cos^2 2\theta)/(1 + \cos^2 2\theta_m)$. If there is a polarization-sensitive analyser crystal following the sample, its relative transmission of X-rays polarized within or perpendicular to its plane of scattering must also be taken into account.

The multiplicity factor m_{hkl} accounts for the number of symmetry-equivalent reflections in the crystal structure, *i.e.*, the number of distinct reflections that have the same structure factor. Note that the equivalence of Bragg reflections depends on the Laue group of the sample. For example, in the cubic space group $Fm\bar{3}m$, reflections (hkl) and (khl) are equivalent, whereas they are not in space group $Fm\bar{3}$. If the atomic scattering factors are purely real or the structure is centrosymmetric, the intensities of Friedel pairs hkl and $\bar{h}\bar{k}\bar{l}$ are equal. However, in an acentric structure with significant imaginary component of any of the atomic scattering factors (see below), Friedel pairs cannot be treated as symmetry equivalent.

The (dimensionless) X-ray structure factor is given by

$$A_{hkl} = \sum_n f_n \exp(2\pi i \mathbf{G}_{hkl} \cdot \mathbf{r}_n) \exp(-W_n) \quad (3.2.3)$$
$$= \sum_n f_n \exp[2\pi i(hx_n + ky_n + lz_n)] \exp(-W_n),$$

where the sum runs over all atoms in the unit cell. In the first form of this equation, $\mathbf{r}_n$ is the vector from the origin of the unit cell to the nth atom; in the second form, x_n, y_n and z_n are fractional coordinates of the nth atom in the unit cell such that $\mathbf{r}_n = x_n\mathbf{a} + y_n\mathbf{b} + z_n\mathbf{c}$.

The term $\exp(-W_n)$ is called the Debye–Waller factor, and it accounts for random dynamical motion of the nth atom away from its equilibrium position. This may be due to thermal fluctuations or (at low temperature) the quantum zero-point motion. If the atomic motion is isotropic, this term takes the form

$$W_n = B\sin^2\theta/\lambda^2 = 8\pi^2 U_n \sin^2\theta/\lambda^2, \quad (3.2.4)$$

where $U_n = \langle u_n^2 \rangle$ is the mean-square fluctuation of the atom's distance from its equilibrium position (in three dimensions). Observed values of B are generally in the range of 0.5 to 1 Å^2 for inorganic crystals, and as large as 5 Å^2 for organic crystals.

A more general treatment of the Debye–Waller factor considers the probability density of the centre of the atom to be a three-dimensional ellipsoidal Gaussian function. Then for a given diffraction peak, it takes the form

$$W = 2\pi^2(U_{11}a^{*2}h^2 + U_{22}b^{*2}k^2 + U_{33}c^{*2}l^2 + 2U_{12}a^*b^*hk + 2U_{23}b^*c^*kl + 2U_{13}a^*c^*hl). \quad (3.2.5)$$

The parameters U_{ij} that define the displacement ellipsoid are constrained to match the point symmetry of the site. For example, an atom that lies on a site of *mmm* symmetry will have the cross terms $U_{12} = U_{23} = U_{13} = 0$.

In equation (3.2.3), f_n is the atomic scattering factor, which arises because X-rays interact with the electrons in the sample, and the strength of that interaction depends both on the magnitude of the scattering vector and the X-ray frequency (wavelength). The electrons are distributed around the nucleus, and so their scattering power decreases with increasing magnitude of the scattering vector. There is also a dependence of the phase and amplitude of the scattering factor on the X-ray energy, which is especially significant near resonance with atomic transition energies. These factors are gathered into the atomic scattering factor f_n, which is commonly written as

$$f_n = f_n^0(\sin\theta/\lambda) + f'(\lambda) + if''(\lambda). \quad (3.2.6)$$

f^0 is the Fourier transform of the electron number density, so that $f^0(0)$ is equal to the number of electrons in the atom or ion. These factors are tabulated in *International Tables for Crystallography*, Volume C, Chapter 6.1 and https://physics.nist.gov/PhysRefData/FFast/html/form.html and http://henke.lbl.gov/optical_constants/asf.html. Values of atomic scattering factors are normally incorporated into data-analysis programs that require them, so the user does not often have to worry about them.

Equation (3.2.3) above is premised on the assumption that the distribution of electrons in the sample is confined to spherically symmetric atoms, *i.e.,* ignoring charge density in bonds and the deformation of core electron density. For the purposes of phase identification and structure refinement, this is generally a good approximation. X-ray determination of non-spherical charge densities goes beyond the scope of this introduction; for further information, see *e.g.* Coppens (1997) and Bindzus *et al.* (2014).

In energy-dispersive X-ray measurements, the detector sits at a fixed 2θ and collects diffracted radiation from a continuum source. The independent variable of the measurement can be taken as the X-ray energy, $E = hc/\lambda$. With the appropriate change of variables, equation (3.2.2) can be written as

$$\frac{d\sigma}{d\Omega} = \frac{Nr_e^2}{16\pi V}\frac{h^3c^3 Pm_{hkl}}{E^2\sin^3\theta}|A_{hkl}|^2\delta\left(E - \frac{hc}{2d\sin\theta}\right). \qquad (3.2.7)$$

Recall that hc = 12.398 KeV Å in convenient units. Again, instrument resolution and sample effects will broaden the peak, but its integrated area is given by the terms preceding the delta-function. Of course, the diffracted intensity must be normalized to the incident spectrum as a function of energy; this may be a rather complicated undertaking as it involves energy-dependent corrections for such factors as detector sensitivity, absorption in the sample *etc.*

3.2.2.2.2. *Neutrons and nuclear scattering*

Neutrons interact with the sample in two ways: the strong interaction with the atomic nuclei, and the magnetic interaction between the neutron's dipole moment and magnetization density in the sample. We consider here only unpolarized neutrons; the use of polarized neutrons permits separation between nuclear and magnetic scattering as well as direct observation of the interference between the two; details are beyond the scope of this chapter. Nuclear scattering is very similar to the X-ray case discussed above, except that the atomic scattering amplitude $r_e f_n$ is replaced by the nuclear coherent scattering length $\bar{b}_n$ (given in *International Tables for Crystallography*, Volume C, Table 4.4.4.1), which is generally independent of neutron energy.

Unlike X-rays, the strength of the neutron–nucleus interaction is not a smooth function of atomic number. This creates opportunities to use neutrons to distinguish atoms with nearly identical X-ray scattering amplitudes, but it also makes certain elements very difficult to study with neutrons. The interaction between neutrons and the nuclei in the sample depends on the isotope and possibly the spin angular momentum of the neutron–nucleus system. This means that incoherent scattering can be significantly larger than the (coherent) diffracted signal for certain atoms, notably hydrogen (^{1}H); see Chapter 2.3 of this volume for further details. For wavelengths of interest in crystallography, the nucleus is essentially a point, and so there is no atomic form factor. This generally leads to greater intensity relative to X-rays at increasing scattering vector (decreasing d-spacing).

Neutron diffractometers operate in one of two ways: angle dispersive or energy dispersive. The configuration for angle-dispersive diffraction measurements is conceptually similar to that used for X-rays; a monochromatic beam of neutrons impinges on the sample and a detector measures the distribution of neutrons *versus* scattering angle. For Bragg neutron diffraction from nuclei,

$$\frac{d\sigma}{d\Omega} = \frac{N\lambda^3}{16\pi V}\frac{m_{hkl}}{\sin\theta\sin 2\theta}|A_{hkl}^{(n)}|^2\delta\left(2\theta - 2\sin^{-1}\frac{\lambda}{2d}\right), \qquad (3.2.8)$$

where the neutron nuclear structure factor is defined as

$$A_{hkl}^{(n)} = \sum_n \bar{b}_n\exp(2\pi i\mathbf{G}\cdot\mathbf{r}_n)\exp(-W). \qquad (3.2.9)$$

Time-of-flight neutron diffractometers, generally based at pulsed spallation sources, operate by measuring the time from the creation of the pulse of neutrons at the target until they appear in a given detector. If the total path length from source to detector is L and the detector is situated at an angle 2θ, a neutron with time of flight t had speed L/t and wavelength $\lambda = ht/m_nL$. Here h is Planck's constant and m_n is the mass of the neutron. This provides a measurement of the d-spacing within the sample, $d = ht/(2m_nL\sin\theta)$. Another change of variables from equation (3.2.2) yields

$$\frac{d\sigma}{d\Omega} = \frac{N}{64\pi V}\left(\frac{h}{m_nL}\right)^3\frac{t^4}{\sin^2\theta}m_{hkl}|A_{hkl}|^2\delta(t - 2d\sin\theta Lm_n/h).$$

$$(3.2.10)$$

In practice, a large number of detectors surround the sample and counts from the same d-spacing (appropriately normalized for incident-beam intensity and detector solid angle) are binned together. In convenient units, $m_n/h = 253\ \mu\text{s m}^{-1}\ \text{Å}^{-1}$.

3.2.2.2.3. *Neutrons and magnetic scattering*

Magnetic neutron scattering is also described through a structure factor which is, however, a vector. The magnetic moment of the neutron interacts with the magnetization density of unpaired electrons in the sample, which may possess spin and/or orbital angular momentum. The magnetic interaction is only sensitive to the component of magnetization perpendicular to the scattering vector. When discussing magnetic scattering, it is more common to use the scattering vector $\mathbf{Q} = 2\pi\mathbf{G}$. The magnetic structure factor is defined as

$$\mathbf{A_Q}^{\text{mag}} = (\gamma r_e/2)\sum_n f_n(Q)(\hat{\mathbf{Q}}\times\mathbf{m}_n\times\hat{\mathbf{Q}})\exp(i\mathbf{Q}\cdot\mathbf{r_n})\exp(-W).$$

$$(3.2.11)$$

Here $\gamma = 1.9132$ is the neutron gyromagnetic factor, $f_n(Q)$ is the atomic magnetic form factor, $\mathbf{m}_n$ is the magnetization of the nth site in units of the Bohr magneton and $\hat{\mathbf{Q}}$ is the unit vector in the direction of $\mathbf{Q}$. The double cross product isolates the component of magnetization perpendicular to $\mathbf{Q}$.

Note that many magnetically ordered materials have a magnetic cell which is larger than the chemical cell. Indeed, many magnetic phases are incommensurately modulated, *i.e.*, the magnetic structure is not periodic with any combination of the chemical unit cell translation vectors. Such matters are beyond the scope of this introduction, and are handled in Chapter 7.13 of this volume.

For unpolarized neutron measurements (*i.e.*, an average over all polarization states of the incoming and diffracted beam), the intensities of the nuclear and magnetic diffraction peaks may be computed separately and then added to determine the overall diffraction pattern. In cases where the chemical and magnetic cells are identical (*e.g.* simple ferromagnets) the nuclear and magnetic diffraction patterns overlap, and so one observes only intensity differences upon magnetic ordering. In the case of antiferromagnets, new magnetic diffraction peaks appear at positions not allowed for the chemical unit cell.

Note also that the magnetic form factor depends on the spin density in the magnetic orbitals, which are typically of greater spatial extent than either the total charge density or the nuclear

density. Therefore, the intensity of magnetic neutron diffraction peaks falls off much more rapidly with $(\sin\theta)/\lambda$ than do nuclear neutron diffraction peaks.

3.2.2.3. *Peak shapes*

The shape of a powder-diffraction peak is a convolution of the intrinsic line shape due to the microscopic structure of the sample crystallites (*e.g.* size and strain) and the configuration of the instrument used to record the pattern. A major goal of powder-diffraction analysis is to be able to separate the contributions of instrument and sample, so that information about the micro-structure of the sample can be extracted reliably. On the other hand, in some cases one simply wants to be able to model the combined influence of instrument and sample, to obtain a func-tional form that permits the most accurate way of apportioning intensities to partially overlapping peaks.

Consider first the sample-dependent factors. The following division into size and strain effects is somewhat artificial, insofar as lattice strains affect the size of the coherently diffracting domain. Nevertheless, it is common to make a distinction between the two, as size broadening produces a peak width proportional to $1/\cos\theta$ in angle-dispersive measurements, whereas the peak width is proportional to $\tan\theta$ for strain broadening.

3.2.2.3.1. *Domain size*

In very general terms, diffraction peaks from an object of linear size L will have a width in Q of the order of $1/L$. As formulated by Scherrer (1918), in an angle-dispersive measure-ment, the full width at half-maximum (FWHM) in 2θ, measured in radians, is given by

$$\Gamma = \frac{K\lambda}{L\cos\theta}, \qquad (3.2.12)$$

where K is called the shape factor and is a number of the order of unity whose precise value depends on the shape of the particles, which are assumed to be of uniform size and shape. The FWHM shape factor for a spherical particle is $K = 0.829$ (Patterson, 1939). Note that if a powder sample is polydisperse (*i.e.*, it contains a distribution of grain sizes), the average grain size is not neces-sarily given by the Scherrer equation.

Perhaps a more useful measure of the width of a peak is the integral breadth. In an angle-dispersive measurement, the inte-gral breadth of a given peak centred at $2\theta_0$ is defined as

$$\beta = \frac{1}{I(2\theta_0)}\int I(2\theta)\,\mathrm{d}2\theta.$$

From a technical point of view, measurement of the integral breadth requires accurate measurement of the intensity in the wings of the diffraction peak, which in turn depends on accurate knowledge of the background intensity.

For any crystallite shape, it can be shown that the integral breadth is related to the volume-average thickness of the crys-tallite in the direction of the diffraction vector, *viz.*

$$L_V = \frac{\lambda}{\beta\cos\theta} = \frac{1}{V}\int \mathrm{d}^3\mathbf{r}\,T(\mathbf{r},\mathbf{G}),$$

where V is the volume of the crystallite and $T(\mathbf{r},\mathbf{G})$ is the length of the line inside the crystallite parallel to $\mathbf{G}$ and passing through the point $\mathbf{r}$. For example, if one writes an integral-breadth version of the Scherrer equation,
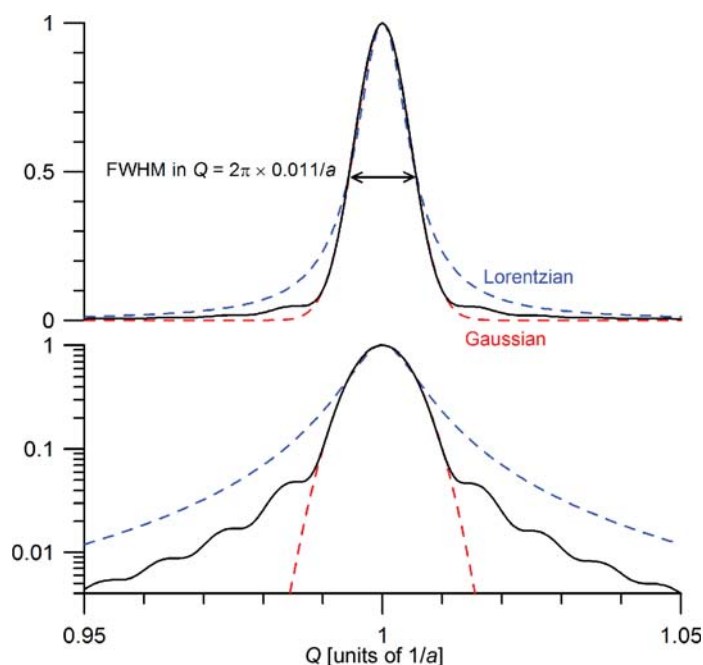

Figure 3.2.1
Computed powder line shape from an ensemble of spherical particles of diameter $100a$, including comparison to Gaussian and Lorentzian line shapes of equal FWHM.

$$\beta = \frac{K_\beta\lambda}{L\cos\theta},$$

the shape factor K_β is unity for $(00l)$ reflections from cube-shaped crystals of size L. $K_\beta = 1.075$ for a sphere of diameter L.

An important feature of the integral breadth is that it has a well defined meaning for a polydisperse sample of crystallites. Assuming that the crystallites all have the same shape,

$$\beta = \frac{K_\beta\lambda\langle L^3\rangle}{\cos\theta\langle L^4\rangle},$$

where $\langle L^3\rangle$ and $\langle L^4\rangle$ are the third and fourth moments of the size distribution (Langford & Wilson, 1978).

In many applications such as Rietveld or profile refinement, it is important to treat the full shape of the diffraction peak instead of merely its width (Loopstra & Rietveld, 1969; Rietveld, 1969). By way of illustration, Fig. 3.2.1 shows one Bragg peak of the computed powder-diffraction pattern from an ensemble of spherical particles of point scatterers in a simple cubic lattice. The lattice parameter is a, and the diameter of the particles is chosen to be $100a$, so that each crystallite consists of approximately 5.2×10^5 'atoms'. (This line shape was calculated using the Debye equation, described in Section 3.2.4.)

Several different analytical functions are frequently used in powder diffraction. In terms of the independent variable x, centred at x_0 with FWHM Γ, the normalized Gaussian function is

$$G(x - x_0) = \pi^{-1/2}\sigma^{-1}\exp-\left(\frac{x-x_0}{\sigma}\right)^2,$$

with $\sigma = \Gamma/2(\ln 2)^{1/2}$. The normalized Lorentzian is

$$L(x - x_0) = \frac{\Gamma/2\pi}{(x-x_0)^2 + (\Gamma/2)^2}.$$

The symmetric Pearson-VII function is a generalization of the Lorentzian, written as

$$P(x - x_0) = \frac{a}{\Gamma}\left[1 + b\left(\frac{x - x_0}{\Gamma}\right)^2\right]^{-m}.$$

Here m is a parameter that governs the line shape (essentially the strength of the wings *versus* the peak), and the numerical parameters $b = 4(2^{1/m} - 1)$ and $a = (b/\pi)^{1/2}\Gamma(m)/\Gamma(m - 1/2)$. (Note the gamma function in the definition of a; the FWHM does not appear in that expression.) The Pearson-VII function with $m = 1$ is a Lorentzian, and it is a Gaussian in the limit $m \to \infty$.

It must be emphasized that none of these functions has any theoretical justification whatsoever. However, in loose powders size broadening is almost always Lorentzian, while Gaussian size broadening is more commonly observed in dense polycrystalline specimens (such as bulk metals).

The Lorentzian and Gaussian functions are also plotted in the same figure for comparison to the actual powder-diffraction line shape of a spherical particle. It can be seen that the correct function has stronger tails than the Gaussian, but the Lorentzian line shape seriously overestimates the intensity in the wings. Both the Gaussian and the Pearson VII fail to capture the general feature that any compact object with a sharp boundary will give a diffraction line shape with tails that asymptotically decay as $(x - x_0)^{-2}$.

One approach to obtaining a more accurate phenomenological description to diffraction line shapes is the Voigt function, which is a convolution of a Gaussian and Lorentzian,

$$V(x - x_0) = \int dx'\, G(x' - x_0)L(x - x').$$

The presence of two shape parameters, the independent widths of the Gaussian and Lorentzian functions, provide independent parameters to control the width and the strength of the wings in the Voigt line shape. The Voigt is more computationally expensive than any elementary function, and so a commonly used approximation is the pseudo-Voigt,

$$PV(x - x_0; \Gamma) = \eta L(x - x_0; \Gamma) + (1 - \eta)G(x - x_0; \Gamma),$$

which is a mixture of Gaussian and Lorentzian functions of the same width. The parameter η controls the shape (strength of the wings) of the pseudo-Voigt line-shape function, independent of its width. There is a computationally convenient approximate relation between Voigt line-shape parameters Γ_L and Γ_G and the pseudo-Voigt Γ and η (Thompson *et al.*, 1987).

3.2.2.3.2. *Strain*

An individual crystal in a sample may be subject to lattice deformation, either due to forces external to that crystal, or to internal factors such as substitutional disorder and dislocations. A comprehensive treatment of microstructural properties and their effects on powder-diffraction peak shapes is given in Chapter 3.6 of this volume; this section gives a general overview from a phenomenological basis.

The simplest description of strain broadening imagines an ensemble of independent crystallites with different lattice parameters. If the crystallites have an isometric distribution of lattice parameters with a fractional width $\delta a/a$, that will be reflected in the range of d-spacings for each reflection. In an angle-dispersive measurement, this will lead to an angular width $\delta 2\theta = 2 \tan \theta\, \delta a/a$ (radians).

Physically plausible mechanisms for a distribution of strains in a powder sample include random inter-grain forces arising during crystallization and the elastic response to internal defects such as dislocations. In practice, these effects often give rise to peak

widths which likewise grow as $\tan \theta$. However, there is no *a priori* basis for expecting any particular functional form for that distribution. Frequent practice is to assume a Gaussian, Lorentzian, Voigt, or pseudo-Voigt form for an isotropic strain broadening, with an adjustable parameter ε representing the FWHM of the strain distribution. The FWHM Γ of the chosen functional form is then $\Gamma_{2\theta} = 2\varepsilon \tan \theta$ for angle-dispersive measurements, $\Gamma_E = \varepsilon E$ for energy-dispersive X-ray measurements and $\Gamma_t = \varepsilon t$ for neutron time-of-flight measurements.

3.2.2.3.3. *Instrumental contributions*

The instrument used to collect diffraction data affects the observed line shape in many ways. A complete discussion is beyond the scope of this article (but see Chapter 3.1, and would have to consider many different diffraction geometries separately. One approach, generally known as fundamental parameters, is to model the effect of every optical element on the peak shape. The instrumental response function is then the convolution of all of these individual contributions.

The simplest (and most widely successful) application of fundamental parameters arises from the analysis of Caglioti *et al.* (1958, 1960) on the instrument response function of a step-scanning powder diffractometer at a reactor neutron source. Neutrons pass through a parallel-blade collimator to a monochromator crystal, through a second collimator to the sample, and then through a third collimator into the detector. It is a fair approximation to assume that the transmission functions of the collimators and the mosaicity of the monochromator are all Gaussians. In that case, the instrument response function produces diffraction peaks which are also Gaussians, with a width that depends on the diffraction angle as

$$\Gamma = \left(U \tan^2 \theta + V \tan \theta + W\right)^{1/2}, \qquad (3.2.13)$$

where the parameters U, V and W can be expressed in closed form as functions of the collimator acceptances and monochromator angle and mosaicity (Caglioti *et al.*, 1958, 1960). Indeed, it was this simple form of the line-shape function that allowed Rietveld and co-workers to develop the important methodology of data analysis commonly known as the Rietveld or profile method (Loopstra & Rietveld, 1969; Rietveld, 1969).

The functional form used to describe the shape of the pulse that emerges from the moderator of a spallation neutron source, and the numerical values of the parameters which go into it, determine the peak shapes observed in the powder diffractometer at such an instrument. The treatment of such matters lies beyond this introduction; documentation of the widely used *GSAS* software includes a detailed description (Larson & Von Dreele, 2004; see also Chapter 3.3).

Analytical treatment of the resolution of X-ray diffractometers is generally complicated by the fact that the various contributions are more difficult to model, especially in the case of the para-focusing Bragg–Brentano geometry most commonly used in laboratory X-ray diffractometers. In the diffractometer, one generally considers factors that affect the line shape separately in the equatorial plane (the plane containing the source, sample and detector) and the axial direction (perpendicular to the equatorial plane, *i.e.*, parallel to the diffractometer axis). In the equatorial plane the resolution is primarily governed by the divergence of the X-ray beam illuminating the sample and by the width of the receiving slit, but there are numerous contributions to the diffraction peak width and shape from such factors as non-conformance of the flat sample surface to the focusing circle,

partial transparency of the sample and misalignment of the diffractometer (Cheary & Coelho, 1992). Even if a monochromator is used to select only the $K\alpha_1$ line, the radiation spectrum from an X-ray tube consists of several Lorentzian functions owing to satellite transitions.

Axial divergence produces a pronounced asymmetry of low-angle diffraction peaks to the low-angle direction (and on the high-angle side of peaks with 2θ near 180°). If the incident or diffracted rays are out of the equatorial plane, they will be intercepted at a detector setting below (above) the actual diffraction angle if it is small (close to 180°), respectively. The effect can be minimized, but not completely eliminated, by narrowing the beam-defining apertures in the equatorial direction, or by introduction of parallel-blade Soller (1924) slits. The full treatment of the effect of axial divergence in a Bragg–Brentano diffractometer has been presented in a computationally convenient form (Cheary & Coelho, 1998).

It is generally easier to model the instrumental response function of a powder X-ray diffractometer based on a synchrotron-radiation source with an analyser crystal, because the transfer functions of the various optical elements are simpler to express. One approach is to approximate the wavelength- and angle-dependent reflectivity of monochromator and analyser crystals by Gaussians, and derive a closed-form expression for the width of the instrument response function (Sabine, 1987). This has been extended to include collimating and focusing (in the scattering plane) mirrors (Gozzo *et al.*, 2006); see Chapter 3.1 for a full description of the relevant optical configurations. A shortcoming of this analytical approach is that the correct single-crystal reflectivity function is not a Gaussian, so it cannot account for the correct line shape, only provide an estimate of its width. Numerical convolutions to accurately model the line-shape function have been performed, and produce excellent agreement with measured profiles (Masson *et al.*, 2003).

Instead of the analytical approach described in the previous few paragraphs, one frequently writes a parametrized function for the measured line shape without concern for the connection between the numerical values of the parameters and the microscopic properties of the sample or the geometry of the diffractometer. For example, one can use the Caglioti form for diffraction peak width [equation (3.2.13)] on any diffractometer, and adjust the parameters U, V and W to some measured standard sample. If size and strain contributions to sample-dependent broadening are both regarded as Lorentzians, they could be combined as $\Gamma = X/\cos\theta + Y\tan\theta$. (Here we make use of the fact that the convolution of two Lorentzians is a Lorentzian whose width is the sum of the individual widths. For Gaussians, the widths combine in quadrature, *i.e.*, $\Gamma^2 = \Gamma_1^2 + \Gamma_2^2$.) In the general case, where neither the instrumental response function nor the sample broadening is purely a Gaussian or Lorentzian function, one can write an empirical line shape as the approximate convolution of a Gaussian and a Lorentzian, with widths given by

$$\Gamma_G = (U\tan^2\theta + V\tan\theta + W + P/\cos^2\theta)^{1/2},$$
$$\Gamma_L = X/\cos\theta + Y\tan\theta. \qquad (3.2.14)$$

This is one of the flexible line-shape models available in the widely used program *GSAS* (Larson & Von Dreele, 2004). It is still possible to make a semi-quantitative statement about sample properties by comparing refined parameters against a standard sample; for example, size broadening will increase the P and X parameters, and strain will increase U and Y. A similar model is used in the *FullProf* software (Rodríguez-Carvajal, 1993, 2001; Kaduk & Reid, 2011).

3.2.3. Complications due to non-ideal sample or instrument properties

In this section, we consider various factors that modify powder X-ray diffraction data relative to the idealized situation described above.

3.2.3.1. *Absorption within a homogeneous sample*

In equations (3.2.2) and (3.2.10), it was assumed that the neither the incident nor the diffracted radiation is absorbed within the sample. However, it is generally the case that neutrons or X-rays are attenuated as they travel through any material, such that the fraction of original intensity surviving after a distance x is $I(x)/I(0) = \exp(-\mu x)$. Here μ is the linear absorption coefficient, which generally depends strongly on the composition of the sample and the X-ray wavelength.

X-ray attenuation coefficients for elements are often given as mass attenuation coefficients, μ/ρ, in units of $cm^2 g^{-1}$. These are available in various sources, such as *International Tables for Crystallography*, Volume C, Table 4.2.4.3, or from internet resources such as http://11bm.xray.aps.anl.gov/absorb/absorb.php. The exact positions of X-ray absorption edges can depend on the chemical environment of the atom, and so tabulated or computed atomic absorption coefficients are not entirely trustworthy within about ± 100 eV of an absorption edge. The X-ray mass attenuation coefficient is related to the imaginary part of the atomic scattering factor [equation (3.2.6)] as $\mu_m = 2r_e\lambda f''/m$, where m is the atomic mass. For a compound or other mixture of elements of total density ρ in which the (dimensionless) mass fraction of element i is g_m^i, the X-ray linear absorption constant is given by

$$\mu_{\text{X-ray}} = \rho \sum_i g_m^i (\mu_m/\rho)^i.$$

In the case of neutrons used for powder diffraction, the absorption cross section is typically tabulated in barns (1 barn = 10^{-24} cm^2); see Table 4.4.4.1 in *International Tables for Crystallography*, Volume C or websites such as http://www.ncnr.nist.gov/resources/n-lengths/list.html. The neutron absorption cross section is generally inversely proportional to velocity, and values are usually tabulated for neutrons with a speed of 2200 m s^{-1} (*i.e.*, 25.3 meV kinetic energy, 1.80 Å wavelength). For neutrons, the equivalent expression with absorption cross sections depends on the number densities g_n^i (atoms/volume) of each element:

$$\mu_{\text{neutron}} = \sum_i g_n^i (\sigma_{\text{abs}}^i + \sigma_{\text{inc}}^i).$$

Considering absorption, the effective volume is given by an integral over the sample,

$$V_{\text{eff}} = \int d^3 \mathbf{R} \exp[-\mu(L_{\text{in}} + L_{\text{out}})], \qquad (3.2.15)$$

where L_{in} and L_{out} are the paths of the incident and diffracted radiation to the point $\mathbf{R}$ within the sample, respectively.

The simplest case is of a sample in the form of a flat plate, with a thickness significantly greater than $1/\mu$, in the dividing position so that the angles of incidence and diffraction from the plane of the sample are both equal to θ. Let the dimensions of the beam be W in the equatorial direction (in the diffraction plane) and H in the axial direction (parallel to the diffractometer axis, *i.e.*, perpendicular to the scattering plane) as shown in Fig. 3.2.2.
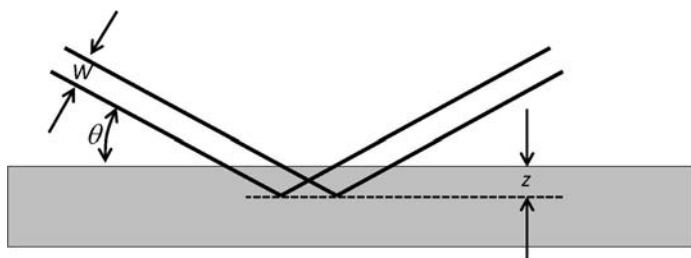
Figure 3.2.2
Sketch illustrating symmetrical diffraction from a flat sample.

Assume that the detector is large enough in the equatorial direction that all diffracted radiation is captured (*i.e.*, no loss of signal due to parallax). Radiation scattered from a volume element a distance z below the surface of the sample will have a total path length $2z/\sin\theta$; integration yields an effective sample volume of $WH/2\mu$, independent of diffraction angle. The situation is more complicated if a flat sample is not optically deep or if the sample is shorter than $W/\sin\theta$; in either case, computation of the effective volume is straightforward, as long as the sample geometry is known with sufficient accuracy. The calculations are described in detail in Chapter 5.4 of this volume.

Another important case is that of a cylindrical sample, such as a Lindemann capillary for X-rays or a can of appropriate material (often vanadium) for neutrons. The integration for V_{eff} above is given in convenient form for computation by Ida (2010), and is tabulated in *International Tables for Crystallography*, Volume C, Section 6.3.3.2. In the case of monochromatic radiation (neutrons or X-rays), for a given absorption constant μ, V_{eff} is an increasing function of diffraction angle 2θ so that higher-angle peaks will appear relatively stronger. Weak-to-moderate absorption from a cylindrical sample affects the observed intensities in essentially the same algebraic form as a negative effective Debye–Waller factor (Hewat, 1979), leading to significantly underestimated (perhaps even negative) measured Debye–Waller factors. In the case of pulsed neutrons, the effect is compounded by the fact that the absorption cross section is generally inversely proportional to the neutron velocity; consequently, in a given detector, faster neutrons, representing larger $|\mathbf{G}|$, will suffer less attenuation in the sample.

3.2.3.2. *Absorption with multiphase samples*

One important application of powder diffraction is the quantitative analysis of mixtures. Quantitative phase analysis is covered in detail in Chapter 3.9 of this volume; here we set the stage. If a sample is a mixture of several phases, the powder-diffraction pattern will be the sum of the patterns of each phase, weighted by the fraction of the illuminated volume occupied by that phase. The most common configuration for quantitative analysis by X-ray diffraction is reflection from an optically deep flat-plate sample. In this case, the integrated intensity of a particular reflection from the jth phase is

$$I_{hkl}(j) = I_0 LP(\theta)\frac{m_{hkl}(j)|A_{hkl}(j)|^2}{V^2(j)}\frac{w_m(j)}{\rho(j)\overline{\mu}}, \qquad (3.2.16)$$

where $V(j)$, $w_m(j)$ and $\rho(j)$ are the unit-cell volumes, mass fraction and density of phase j, respectively. Here I_0 is an overall intensity scale factor, $LP(\theta)$ is the Lorentz and polarization factor common to all phases, and $\overline{\mu} = \sum_j w_m(j)\mu(j)$ is the absorption coefficient

of all solid phases in the sample. The summation includes all solid phases, even amorphous materials.

Note that the intensity of peaks from a particular phase is not simply proportional to the fraction of that phase present. For example, if there are two phases A and B, the intensity of A peaks will be proportional to

$$\frac{w_m(A)}{w_m(A)[\mu(A) - \mu(B)] + \mu(B)}.$$

3.2.3.3. *Granularity, microabsorption and surface roughness*

The above discussion of absorption in a powder sample is premised on the assumption that the powder sample is sufficiently fine that the beam traverses a large number of grains, *i.e.*, that $\mu\ell \ll 1$, where μ is the absorption coefficient in the solid material and ℓ is a characteristic linear grain dimension. In that case, the effective linear absorption constant is $\overline{\mu} = \mu\rho_{powder}/\rho_{solid}$, independent of the path that the radiation follows through the sample. However, if $\mu\ell$ is not very small, the simple picture of an average absorption length in the sample breaks down, leading to changes in the diffracted intensity.

There have been several treatments of microabsorption due to porosity and surface roughness. Rather than reviewing the literature, this section summarizes work of Hermann & Ermrich (1987) on a flat sample in the symmetrical reflection geometry discussed above. The single-phase sample is taken to be a collection of random polyhedra of average chord length ℓ with packing fraction α_0. The surface has the same lateral correlation length, but the average packing fraction rises from zero at the surface with characteristic dimension t_s, *i.e.*, $\alpha(z) = \alpha_0[1 - \exp(-z/t_s)]$, where z is the distance from the surface into the sample. $t_s = 0$ represents an abrupt termination of the bulk porous material.

Hermann & Ermrich find that the diffracted intensity is reduced from the fine powder limit by a factor of $1 - P_{bulk} - P_{surface}$, where

$$P_{bulk} \simeq 2\mu\ell(1 - \alpha_0)^2,$$

$$P_{surface} \simeq \frac{2\mu\alpha_0 t_s}{\sin\theta}\left(1 - \frac{t_s}{\ell(1 - \alpha_0)\sin\theta}\right).$$

If surface roughness is small, there is no dependence on diffraction angle 2θ, and the only effect is an overall reduction of diffracted intensity. Excess surface roughness ($t_s > 0$), as might be produced by allowing a granular powder to settle against a flat surface, leads to additional diminution of diffracted intensity at low angles. The expression for $P_{surface}$ given above is to leading order in $1/\sin\theta$, and is therefore not valid for small grazing angles of incidence. Note that both the surface and bulk correction factors approach zero as $\mu\ell \to 0$. This analysis is in general agreement with analysis and measurements performed by Suortti (1972).

An additional effect of microabsorption in multi-component powders has been considered by Brindley (1945). The principle is illustrated in Fig. 3.2.3. An X-ray propagating through the sample (depicted by the broken line) suffers absorption according to the weighted average $\overline{\mu}$, but an X-ray diffracted in a grain of phase a has travelled further in that phase than average (solid line). If its path in the diffracting grain is x and the total path through the sample is L, absorption will reduce its intensity by a factor

$$\exp(-\mu_a x)\exp[-\overline{\mu}(L - x)].$$
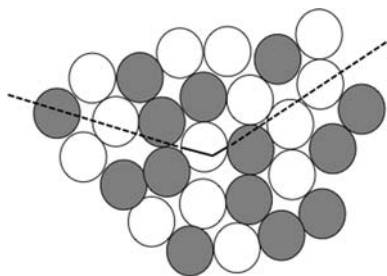
Figure 3.2.3
Sketch illustrating an X-ray propagating through a mixture of two kinds of particles.

This leads to a weaker observed reflection from a phase a with larger absorption constant μ_a if the particle size is an appreciable fraction of $1/(\mu_a - \bar{\mu})$.

Averaging over the particle volume, we see that the observed intensity of phase a will be lowered from its value in a fine powder by a factor

$$\tau = V_a^{-1} \int \exp[-(\mu_a - \bar{\mu})x] \, dV_a,$$

where the integral is taken over one representative grain of phase a. This is exactly the integral of equation (3.2.15), and if one assumes monodisperse spherical particles, it is tabulated in *International Tables for Crystallography*, Volume C, Section 6.3.3.2 and elsewhere, with $\mu_a - \bar{\mu}$ replacing μ. One hitch is that the tabulations are for $\mu > 0$, whereas $\mu_a - \bar{\mu} < 0$ for the less absorbing phases in a mixture. Brindley handles this with a series expansion and provides a table of τ *versus* $(\mu_a - \bar{\mu})R$.

By way of illustration, consider a mixture of equal weight fractions of corundum, magnetite and zircon powders, analysed with Cu $K\alpha$ radiation. Fig. 3.2.4 shows the weight fractions that would be measured from such a sample as a function of particle radius (assumed equal for all three phases). In this case, microabsorption biases the result by about 10% for particles of 10 μm diameter, and misses by a factor of two if the diameter is 70 μm.

In considering microabsorption, there are several important points to note. This entire analysis is only valid for $\mu R \ll 1$, since otherwise the concept of an average absorption length becomes ill defined. That means that the Brindley analysis breaks down precisely when it becomes significant. Of course, the Brindley assumption of monodisperse spherical particles is unrealistic for most real samples. Both the surface roughness and Brindley corrections depend on diffraction angle as well as μR, but, as noted above, for moderate absorption, the angle dependence appears as an effective Debye–Waller factor. The parameter R is the radius of the grain of material, which is commonly very much larger than the size of a coherently diffracting region; a Scherrer analysis of particle size through line broadening does not provide a useful estimate of R. Most importantly, unless one has an accurate independent measurement of the size and shape of the grains, microabsorption corrections should be taken as a sign of impending trouble, not a quantitative correction.

3.2.3.4. *Anisotropic strain broadening*

Strain broadening is often observed not to be monotonically dependent on the magnitude of the d-spacing, but to have a more complicated dependence on the direction of the diffraction vector **G**. An illustration of the effect in cubic Rb_3C_{60} is shown in Fig. 3.2.5 (Stephens, 1999). The lower part of the figure shows an apparently irregular trend of diffraction peak widths on diffraction angle 2θ.
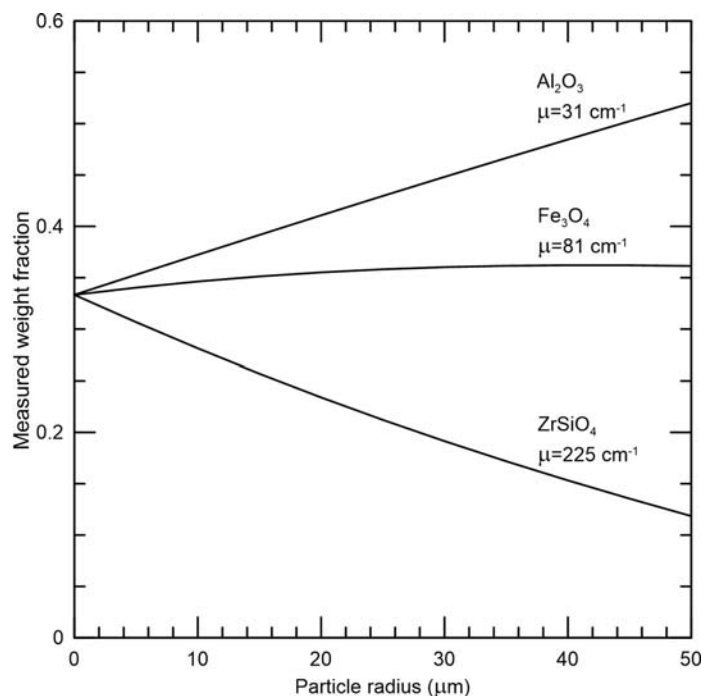
Figure 3.2.4
Weight fractions that would be measured from a mixture of equal parts of three phases with Cu $K\alpha$ radiation.
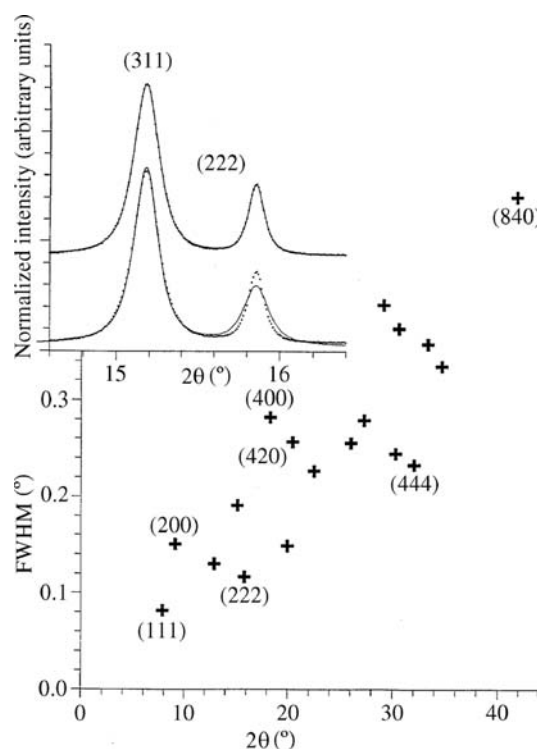
Figure 3.2.5
Diffraction peak width *versus* diffraction angle from a powder pattern of face-centred cubic Rb_3C_{60} (Stephens, 1999). The inset at the top shows a limited range of the data, fitted by a model with two different peak widths (upper trace) and with the widths constrained to be equal (lower trace).

Whatever the nature of random internal stresses and strains, it can be argued on quite general grounds that strain broadening depends on a combination of fourth-rank tensors. On the assumption that the distribution of internal strains is Gaussian, each diffraction peak has Gaussian shape, and the variance of the inverse d-spacing squared is a quartic form in the reflection indices (hkl), This can be expressed as

$$\langle 1/d^2 \rangle = \sum_{HKL} S_{HKL} h^H k^K l^L, \qquad (3.2.17)$$

where the sum is over terms with $H + K + L = 4$. This leads to a contribution to the width of a diffraction peak given by $\Gamma_{2\theta} = d^4 \langle 1/d^2 \rangle^2 \tan\theta$ for angle-dispersive measurements, and $\Gamma_t = t d^2 \langle 1/d^2 \rangle^2$ for time-of-flight neutron measurements. Strain broadening in real samples frequently leads to peak shapes that are closer to Lorentzian than Gaussian, and the justification of this expression breaks down, because the second moment of the distribution of $1/d^2$ is then not defined. Nevertheless, this method is often successful to model the phenomenology of anisotropic peak broadening.

The parameters S_{HKL} arise from the nature of the strain and the values of elastic constants for any particular sample. Typically, they must therefore be regarded as phenomenological, and can be adjusted in fitting a model to observed data. They are constrained by the symmetry of the Laue group of the sample, which leads to restrictions on the S_{HKL} terms for the various Laue classes, listed in Table 3.2.1 (Popa, 1998).

3.2.3.5. *Preferred orientation (texture)*

The discussion of diffraction-peak intensities in Section 3.2.2.2 above presumes that the sample is a random powder, with every orientation equally probable. Real samples frequently exhibit some deviation from that ideal case, perhaps because of the way that grains of platy or acicular (needle-like) habit settle into a sample holder, or because a solid polycrystalline sample crystallized or grew anisotropically, or was formed or worked as a solid. The latter case is generally called texture, and can provide a fruitful basis for understanding the history or mechanical properties of a sample. The topic is further discussed in Chapter 5.3 of this volume. For the present purposes, deviation from a collection of randomly oriented grains will be regarded as an artifact to be minimized and/or modelled.

The distribution of orientations of crystallites in a sample can be studied using pole figures. For a given reflection $\mathbf{G}$, the pole figure is defined as the probability density over a spherical surface that $\mathbf{G}$ falls in a particular direction relative to the sample. For a random powder, all pole figures would be uniform; for a single crystal, each pole figure would be a set of delta functions. Modelling of preferred orientation in the sample is accomplished by multiplying the theoretical intensity by the pole-figure density in the direction of the diffraction vector. Here we discuss two different treatments of preferred orientation.

The symmetrized spherical-harmonic approach follows Järvinen (1993), considering samples that are axially symmetric about some axis $\mathbf{P}$. Experimentally, this can be ensured by rotating the sample about $\mathbf{P}$ during data collection. Take α to be the angle between $\mathbf{P}$ and the diffraction vector: α is zero for a conventional symmetrical flat plate and 90° for a Debye–Scherrer geometry.

For a given reflection hkl, the polar-axis density in the diffraction direction may be expanded in spherical harmonics as

$$A(hkl, \alpha) = \sum_{ij} C_{ij} Y_{ij}(\theta_{hkl}, \varphi_{hkl}) P_i(\cos\alpha),$$

where Y_{ij} and P_i are the usual spherical harmonics and Legendre polynomials, and θ_{hkl} and φ_{hkl} are the spherical coordinates of the hkl reflection relative to some chosen axis of the crystal.

In general, there will be several reflections equivalent to hkl by the Laue symmetry of the crystalline phase, and so symmetry-adapted functions should replace the spherical harmonics in the

Table 3.2.1

Restrictions and reflections of anisotropic strain parameters for the various Laue classes

$\bar{3}, \bar{3}m1, \bar{3}1m$: hexagonal indices.

Class	$\langle 1/d^2 \rangle^2$
$\bar{1}$	$S_{400}h^4 + S_{040}k^4 + S_{004}l^4 + S_{220}h^2k^2 + S_{202}h^2l^2$ $+ S_{022}k^2l^2 + S_{310}h^3k + S_{130}hl^3 + S_{301}h^3l + S_{103}hl^3$ $+ S_{031}k^3l + S_{013}kl^3 + S_{211}h^2kl + S_{121}hk^2l + S_{112}hkl^2$
$2/m$ (*b*-axis unique)	$S_{400}h^4 + S_{040}k^4 + S_{004}l^4 + S_{220}h^2k^2 + S_{202}h^2l^2$ $+ S_{022}k^2l^2 + S_{301}h^3l + S_{103}hl^3 + S_{121}hk^2l$
$2/mmm$	$S_{400}h^4 + S_{040}k^4 + S_{004}l^4 + S_{220}h^2k^2 + S_{202}h^2l^2 + S_{022}k^2l^2$
$4/m$	$S_{400}(h^4 + k^4) + S_{004}l^4 + S_{220}h^2k^2 + S_{202}(h^2 + k^2)l^2$ $+ S_{310}(h^3k - hk^3)$
$4/mmm$	$S_{400}(h^4 + k^4) + S_{004}l^4 + S_{220}h^2k^2 + S_{202}(h^2 + k^2)l^2$
$\bar{3}$	$S_{400}(h^2 + k^2 + hk)^2 + S_{202}(h^2 + k^2 + hk)l^2 + S_{004}l^4$ $+ S_{211}(h^3 - k^3 + 3h^2k)l + S_{121}(-h^3 + k^3 + 3hk^2)l$
$\bar{3}m1$	$S_{400}(h^2 + k^2 + hk)^2 + S_{202}(h^2 + k^2 + hk)l^2 + S_{004}l^4$ $+ S_{301}(2h^3 + 3h^2k - 3hk^2 - 2k^3)l$
$\bar{3}1m$	$S_{400}(h^2 + k^2 + hk)^2 + S_{202}(h^2 + k^2 + hk)l^2 + S_{004}l^4$ $+ S_{211}(h^2k + hk^2)l$
Hexagonal	$S_{400}(h^2 + k^2 + hk)^2 + S_{202}(h^2 + k^2 + hk)l^2 + S_{004}l^4$
Cubic	$S_{400}(h^4 + k^4 + l^4) + S_{220}(h^2k^2 + h^2l^2 + k^2l^2)$

above equation. Only even orders i are considered, because of the inversion symmetry of diffraction (neglecting imaginary atomic scattering amplitudes). The Laue symmetry of the crystalline phase implies that certain of the harmonics are zero; see the original article by Järvinen (1993) for explicit functional forms of the harmonics and a tabulation of which are allowed for each Laue group.

The second approach considered here is the widely used March (1932)–Dollase (1986) model, which is applicable to the most common powder-diffraction sample geometries of axial symmetry either along the diffraction vector or perpendicular to the diffraction plane, for samples whose preferred orientation arises from the settling of either disc- or rod-shaped crystallites in the sample holder. The cylinder axis $\mathbf{H}$ governs the preferred orientation. For any Bragg reflection $\mathbf{G}$, the pole density in the diffraction direction is hypothesized to be a particular function of the angle α between $\mathbf{H}$ and $\mathbf{G}$, *viz.*

$$A(G) = (R^2 \cos^2\alpha + \sin^2\alpha/R)^{-3/2}.$$

Here R is a parameter describing the degree of preferred orientation; it is less than unity for maximum pole density at $\alpha = 0$, *i.e.*, $\mathbf{H} \parallel \mathbf{G}$, as would be found for disc-like samples preferentially lying in the reflection plane. $R > 1$ corresponds to maximum pole density at $\alpha = 90°$, as might be found for acicular crystallites in either a flat-plate or Debye–Scherrer geometry. The particular functional form has some theoretical justification as a model for grain rotation in settling of a granular sample, as well as being properly normalized, suitable for oblate or prolate grains with a single parameter, and in agreement with pole distributions observed in many samples. To apply this model to powder-diffraction data, one must find the appropriate axis $\mathbf{H}$, either through prior knowledge of growth habit or by trial and error.

3.2.3.6. *Extinction*

The analysis of diffracted intensities in this chapter has been premised on the assumption that the diffracted beam produced by each crystallite is much weaker than the incident beam, known
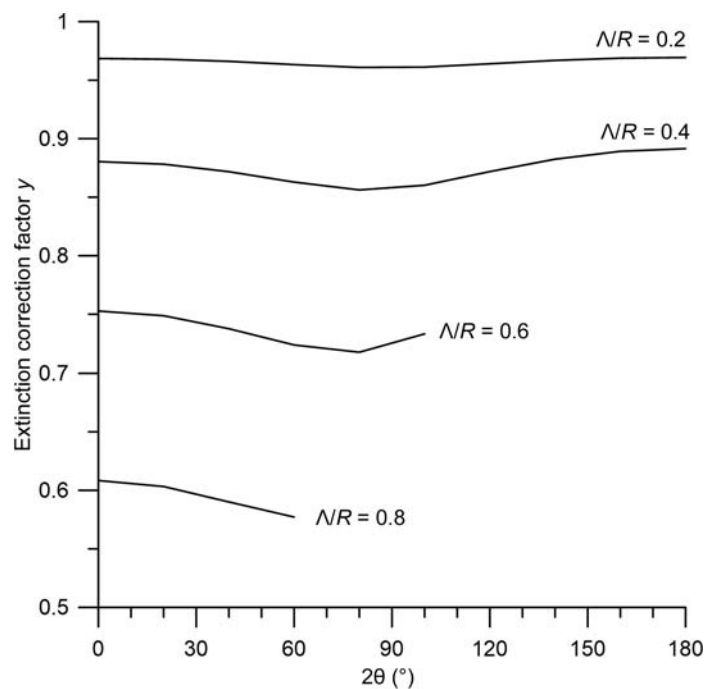
Figure 3.2.6
Extinction correction for spherical particles according to Thorkildsen & Larsen (1998).

as the kinematic approximation. This is a consequence of the Born approximation, whereby the diffracted intensity from one grain is proportional to the number of atoms within it. However, as the size of the crystallite grows, so will the intensity of the diffracted wave within it. The diffracted radiation will be re-diffracted back into the incident beam, leading to a measured integrated intensity less than the kinematic value, by a ratio $y(\mathbf{G}) = I_{\text{obs}}(\mathbf{G})/I_{\text{kinematic}}(\mathbf{G})$, which depends on the particular Bragg reflection $\mathbf{G}$. This is the phenomenon of primary extinction, which can be understood within the framework of the dynamical theory of diffraction. The following discussion ignores absorption.

The relevant physical parameter is the extinction length Λ. For X-rays,

$$\Lambda(\mathbf{G}) = \frac{V}{r_e \lambda P |A_{\mathbf{G}}|},$$

where V is the unit-cell volume, $r_e = 2.82 \times 10^{-15}$ m, $A_{\mathbf{G}}$ is the structure factor, and P is the polarization factor: 1 or $\cos^2 2\theta$ for S or P polarization, respectively. For neutrons,

$$\Lambda(\mathbf{G}) = \frac{V}{\lambda |A_{\mathbf{G}}^{(n)}|}.$$

As an example, the 111 reflection of Si has an extinction length of 7.2 µm for 1.54 Å X-rays and 50 µm for 1.59 Å neutrons. Intensities from the kinematic theory are correct in the limit that the coherent grain size is much less than Λ. Note that extinction is most significant for the strongest reflections in a powder-diffraction pattern.

There are no exact calculations of extinction available for sample geometries applicable to powder samples, but Thorkildsen and Larsen have obtained a rigorous series solution for spherical particles of radius R in powers of Λ/R (Thorkildsen & Larsen, 1998). To lowest order,

$$y = 1 - (R/\Lambda)^2 f_1(\theta), \quad \text{where}$$

$$f_1(\theta) = \frac{8}{5\pi \sin 2\theta}(1 + \pi\theta - 4\theta^2 - \cos 4\theta - \theta \sin 4\theta)$$

$$\text{for } 0 \leq \theta \leq \pi/4$$

$$= \frac{4}{5\pi \sin 2\theta}(2 - \pi^2 + 6\pi\theta - 8\theta^2 - 2\cos 4\theta + \pi \sin 4\theta$$

$$- 2\theta \sin 4\theta) \text{ for } \pi/4 \leq \theta \leq \pi/2.$$

This first term gives y accurate to 3% for $R/\Lambda \leq 0.4$. Fig. 3.2.6 shows their calculated result up to fifth order.

3.2.4. The Debye scattering equation

The Debye scattering equation is an alternative method to compute the diffraction pattern of a collection of solid grains, which does not rely on a requirement of crystalline periodicity (Debye, 1915). Consequently, it is useful for cases where the grains of the sample are not fragments of idealized crystals, such as are frequently observed in nanoparticles. For a collection of identical grains, each containing N atoms having individual scattering amplitude b_j, $1 \leq j \leq N$, the orientation-average cross section per grain is given by

$$\left\langle \frac{d\sigma}{d\Omega} \right\rangle_{\text{orientation}} = \sum_j^N b_j^2 + \sum_j^N \sum_{k \neq j}^N b_j b_k \frac{\sin(2\pi q r_{ij})}{2\pi q r_{ij}},$$

where r_{jk} is the distance between atoms j and k, and the scattering vector $q = 2\sin\theta/\lambda$. For neutrons, b_j is the scattering length; in the case of multiple isotopes of a given atomic species, one may use the coherent scattering length to obtain the coherent elastic cross section. For X-rays, $b_j = r_e f_j(\sin\theta/\lambda)$, the classical electron radius times the atomic scattering factor, and the cross section must be multiplied by the polarization factor as described in Section 3.2.2.2.1. This topic is treated in much greater detail in Chapters 3.6, 5.6 and 5.7 of this volume.

3.2.5. Summary

Although a powder-diffraction experiment is simple experimentally, considerable physics goes into determining the actual experimental data. Any user attempting to extract the maximum information from the diffraction data (especially through a Rietveld refinement) ultimately needs to understand all of the factors that affect the experimental data. This chapter provides a succinct summary of the major factors that contribute to the experimental data. Many of these factors are explored in more detail in other chapters of this volume.

References

Bindzus, N., Straasø, T., Wahlberg, N., Becker, J., Bjerg, L., Lock, N., Dippel, A.-C. & Iversen, B. B. (2014). *Experimental determination of core electron deformation in diamond. Acta Cryst.* A**70**, 39–48.

Brindley, G. W. (1945). *The effect of grain or particle size on x-ray reflections from mixed powders and alloys, considered in relation to the quantitative determination of crystalline substances by x-ray methods. Philos. Mag.* **36**, 347–369.

Caglioti, G., Paoletti, A. T. & Ricci, F. P. (1958). *Choice of collimators for a crystal spectrometer for neutron diffraction. Nucl. Instrum. Methods*, **3**, 223–228.

Caglioti, G., Paoletti, A. & Ricci, F. P. (1960). *On resolution and luminosity of a neutron diffraction spectrometer for single crystal analysis. Nucl. Instrum. Methods*, **9**, 195–198.

Cheary, R. W. & Coelho, A. (1992). *A fundamental parameters approach to X-ray line-profile fitting. J. Appl. Cryst.* **25**, 109–121.

Cheary, R. W. & Coelho, A. A. (1998). *Axial divergence in a conventional X-ray powder diffractometer. I. Theoretical foundations*. *J. Appl. Cryst.* **31**, 851–861.

Coppens, P. (1997). *X-ray charge densities and chemical bonding*. Oxford: International Union of Crystallography/Oxford University Press.

Debye, P. (1915). *Zerstreuung von Röntgenstrahlen. Ann. Phys.* **351**, 809–823.

Dollase, W. A. (1986). *Correction of intensities for preferred orientation in powder diffractometry: application of the March model*. *J. Appl. Cryst.* **19**, 267–272.

Gozzo, F., De Caro, L., Giannini, C., Guagliardi, A., Schmitt, B. & Prodi, A. (2006). *The instrumental resolution function of synchrotron radiation powder diffractometers in the presence of focusing optics*. *J. Appl. Cryst.* **39**, 347–357.

Hermann, H. & Ermrich, M. (1987). *Microabsorption of X-ray intensity in randomly packed powder specimens. Acta Cryst.* A**43**, 401–405.

Hewat, A. W. (1979). *Absorption corrections for neutron diffraction. Acta Cryst.* A**35**, 248.

Ida, T. (2010). *Efficiency in the calculation of absorption corrections for cylinders*. *J. Appl. Cryst.* **43**, 1124–1125.

Järvinen, M. (1993). *Application of symmetrized harmonics expansion to correction of the preferred orientation effect*. *J. Appl. Cryst.* **26**, 525–531.

Kaduk, J. A. & Reid, J. (2011). *Typical values of Rietveld instrument profile coefficients*. *Powder Diffr.* **26**, 88–93.

Krivoglaz, M. A. (1969). *Theory of X-ray and thermal-neutron scattering by real crystals.* New York: Plenum Press. (Translated from the Russian by S. Moss.)

Langford, J. I. & Wilson, A. J. C. (1978). *Scherrer after sixty years: a survey and some new results in the determination of crystallite size*. *J. Appl. Cryst.* **11**, 102–113.

Larson, A. C. & Von Dreele, R. B. (2004). *General Structure Analysis System (GSAS)*. Los Alamos National Laboratory Report LAUR 86–748. Los Alamos, USA.

Loopstra, B. O. & Rietveld, H. M. (1969). *The structure of some alkaline-earth uranates. Acta Cryst.* B**25**, 787–791.

March, A. (1932). *Mathematische Theorie der Regelung nach der Korngestah bei affiner Deformation. Z. Kristallogr.* **81**, 285–297.

Marshall, W. & Lovesey, S. W. (1971). *Theory of Thermal Neutron Scattering.* Oxford: Clarendon.

Masson, O., Dooryhée, E. & Fitch, A. N. (2003). *Instrument line-profile synthesis in high-resolution synchrotron powder diffraction*. *J. Appl. Cryst.* **36**, 286–294.

Patterson, A. L. (1939). *The Scherrer formula for X-ray particle size determination. Phys. Rev.* **56**, 978–982.

Popa, N. C. (1998). *The (hkl) dependence of diffraction-line broadening caused by strain and size for all Laue groups in Rietveld refinement*. *J. Appl. Cryst.* **31**, 176–180.

Riello, P., Fagherazzi, G., Clemente, D. & Canton, P. (1995). *X-ray Rietveld analysis with a physically based background*. *J. Appl. Cryst.* **28**, 115–120.

Rietveld, H. M. (1969). *A profile refinement method for nuclear and magnetic structures*. *J. Appl. Cryst.* **2**, 65–71.

Rodríguez-Carvajal, J. (1993). *Recent advances in magnetic structure determination by neutron powder diffraction. Phys. B Condens. Matter*, **192**, 55–69.

Rodríguez-Carvajal, J. (2001). *Recent developments of the program FULLPROF. IUCr Commission on Powder Diffraction Newsletter*, **26**, 12–19.

Sabine, T. M. (1987). *The N-crystal spectrometer*. *J. Appl. Cryst.* **20**, 23–27.

Scherrer, P. (1918). *Bestimmung der Grösse und der inneren Struktur von Kolloidteilchen mittels Röntgenstrahlen. Nachr. Ges. Wiss. Göttingen*, pp. 98–100.

Smith, D. K. (2001). *Particle statistics and whole-pattern methods in quantitative X-ray powder diffraction analysis. Powder Diffr.* **16**, 186–191.

Soller, W. (1924). *A new precision X-ray spectrometer. Phys. Rev.* **24**, 158–167.

Stephens, P. W. (1999). *Phenomenological model of anisotropic peak broadening in powder diffraction*. *J. Appl. Cryst.* **32**, 281–289.

Suortti, P. (1972). *Effects of porosity and surface roughness on the X-ray intensity reflected from a powder specimen*. *J. Appl. Cryst.* **5**, 325–331.

Thompson, P., Cox, D. E. & Hastings, J. B. (1987). *Rietveld refinement of Debye–Scherrer synchrotron X-ray data from Al$_2$O$_3$*. *J. Appl. Cryst.* **20**, 79–83.

Thorkildsen, G. & Larsen, H. B. (1998). *Primary extinction in cylinders and spheres. Acta Cryst.* A**54**, 172–185.

references